Article

Synergistic Effect in Ag/Fe–MnO$_2$ Catalysts for Ethanol Oxidation

Ekaterina V. Kulchakovskaya [1], **Svyatoslav S. Dotsenko** [1], **Leonarda F. Liotta** [2,*], **Valeria La Parola** [2], **Sergey I. Galanov** [1], **Olga I. Sidorova** [1] **and Olga V. Vodyankina** [1,*]

[1] Laboratory of Catalytic Research, Department of Chemistry, Tomsk State University, 634050 Tomsk, Russia
[2] Istituto per lo Studio dei Materiali Nanostrutturati (ISMN)-CNR, Via Ugo La Malfa 153, I-90146 Palermo, Italy
[*] Correspondence: leonardafrancesca.liotta@cnr.it (L.F.L.); vodyankina_o@mail.ru (O.V.V.)

Abstract: Here we report the synergistic effect of OMS-2 catalysts tested in ethanol oxidation, and the effects produced by both the addition of an Fe modifier in the catalyst preparation stage, and the introduction of Ag on its surface by the impregnation method. To analyze the action of each component, the Fe-modified, Ag-containing OMS-2 catalysts with different Mn/Fe ratios were prepared. Combined XPS and XRF elemental analysis confirms the states and distribution of the Ag- and Fe-containing species between the surface and bulk of the OMS-2 catalysts, which form highly dispersed Ag species on the surface of 0.05Fe–OMS-2, and are also incorporated into the OMS-2 crystalline lattice. The cooperative action of Ag and Fe modifiers improves both reoxidation ability (TPO results) and the amount of adsorbed oxygen species on the catalyst surface. The introduction of Ag to the OMS-2 and 0.05 Fe–OMS-2 surface allows a high level of activity (T_{80} = 150–155 °C) and selectivity (S_{Ac80} = 93%) towards the acetaldehyde formation.

Keywords: silver catalysts; Fe-modified OMS-2; synergistic effect; H$_2$(CO)–TPR/TPO; ethanol oxidation

1. Introduction

Selective oxidation reactions involving heterogeneous catalysts are widely used in industrial processes, e.g., oxidation of methanol, ethylene glycol, ethylene, etc., and synthetic organic chemistry [1,2]. Since bioethanol is one of the potential sources for the production of hydrogen and industrial chemicals, such as acetaldehyde, the development of new catalysts for ethanol conversion is essential. The main advantages of vapor-phase selective ethanol oxidation in comparison with the liquid-phase processes are the use of air as a "green" oxidant, the process implementation at atmospheric pressure, and the simple isolation of acetaldehyde from the reaction products without time-consuming solvent treatment. All catalysts used for selective ethanol oxidation may be separated into two groups: the first includes those catalysts based on transition metal oxides such as vanadium oxide supported by TiO$_2$ [3,4], and the second is constituted of noble metal nanoparticles supported by oxides/nitrides, e.g., supported Au catalysts [5,6], Ag/CeO$_2$ [7], Ag/Si$_3$N$_4$ [8], etc. In 2001, crystalline microporous manganese oxide combined with OMS-2 was introduced as an inexpensive, efficient, ecofriendly, selective catalyst for the oxidation of alcohols in the presence of O$_2$ from air [9]. Taking into account the economic trends and environmental concerns, the application of manganese oxides attracted significant consideration due to the following advantages: low cost, environmental friendliness, ion-exchange properties, mild acid–base stability, and redox activity [10–12]. Manganese oxide, with the structure of octahedral molecular sieves (OMS-2), possesses a one-dimensional (0.46 nm × 0.46 nm) tunnel structure, and consists of three mixed valence states, i.e., Mn(II), Mn(III), and Mn(IV), with the average oxidation state being +3.88 [13]. Thus, materials based on manganese oxide with the OMS-2 structure are the most promising candidates for different applications, e.g., energy storage [14], battery electrodes [15], supercapacitors [16], sewage treatment [17], degradation of organic dyes [18], and catalysis, including benzene oxidation [19], dimethyl

ether combustion [20,21], low-temperature CO oxidation [22], ozone decomposition [23], gas-phase selective ethanol oxidation [24,25], etc.

The structural defects, especially the surface ones, including oxygen vacancies, are the key sites that provide the high level of activity of the oxide catalysts in the redox processes. The enhanced activity of the catalytic OMS-2-based composites is mainly determined by the Mn^{3+}/Mn^{4+} ratio [19]. The introduction of transition metal cations (e.g., Co, Cu, Ni, Cr, Fe, Zn, etc.) to substitute K inside the tunnels, or Mn^{3+}/Mn^{4+} in the octahedral positions, while keeping the initial tunnel structure of α-MnO_2, is one of the main approaches to enhance the oxidative activity of such materials [26,27]. The modifier cations change the concentration of anionic defects, due to the lattice disturbance and changing of the electronic balance of the system [28].

Iron-containing modifiers are promising candidates to enhance the catalytic performance of the MnO_2-based catalysts in oxidative processes. Iron oxides (e.g., Fe_2O_3) are materials with high bulk oxygen utilization, as recently reported for high-index {113} facets of α-Fe_2O_3 [29]. The main drawback of Fe_2O_3 is its low oxygen-conducting rate, which limits its application in low-temperature oxidative reactions. Iron–manganese mixed oxide catalysts were studied in catalytic combustion of ethanol [30], SCR NOx [31], etc. The catalytic activity of such materials was found to be greatly influenced by the Mn/Fe ratio of the formed mixed oxide [30]. Since the catalytic oxidation of organic compounds using OMS-2 catalysts usually proceeds via the Mars–van Krevelen mechanism, implying that organic molecules adsorbed on the catalyst surface are oxidized by a labile surface oxygen; the resultant oxygen vacancies are subsequently replenished by the gas-phase O_2. Thus, promoting the surface oxygen reactivity is a critical point.

It is well-known that silver can adsorb and activate gaseous O_2 to yield O-containing species that can be active in the selective oxidation processes, such as methanol oxidation into formaldehyde, ethylene glycol oxidation into glyoxal, ethylene epoxidation, etc. [32]. Due to the unique surface properties and practically similar ionic radii of K^+ and Ag^+ [33], providing the opportunity for K^+ substitution in the K–OMS-2 tunnels by silver ions, the Ag addition on the MnO_2 surface is thought to be an effective means to improve the catalytic oxidation efficiency of the catalyst. Silver is known as an attractive catalyst for many heterogeneous catalytic oxidation reactions, such as the oxidation of CO at ambient temperature [34,35], formaldehyde [36,37], and benzene [38], the combustion of mobile-derived pollutants [39], and the oxidation of alcohols [35,40,41], etc. The performance of silver-based catalysts depends on their surface structure and composition, thus, it can be modulated by different Ag–O interactions [42]. In addition to their ability to activate molecular oxygen, the silver-based catalysts attract special interest, due to a number of valuable features of the metal, such as homogeneous distribution of metal particles/clusters in various supports (e.g., SiO_2, CeO_2, Mn_xO_y, Si_3N_4, TiO_2, etc.) and synergistic action with a large number of promoters and modifiers (noble metals, transition metal oxides, halogen-containing compounds, etc.) [41,43].

The aim of the present work was to investigate the effect of cooperative action of Fe^{3+} and silver on the physical and chemical properties of OMS-2 catalysts, and their catalytic activity in selective ethanol oxidation into acetaldehyde.

2. Results and Discussion

2.1. XRD and XPS Results

Figures 1 and S1 display the XRD patterns for the prepared samples. All the diffractograms are characteristic of low-crystalline structures, and the identification of the phases is relatively hard. The reflections of {110} and {200} planes typical for manganese oxide with the OMS-2 structure (JCDPS 29-1020), most likely the β-MnO_2 phase (Figure S1), are detected [44].
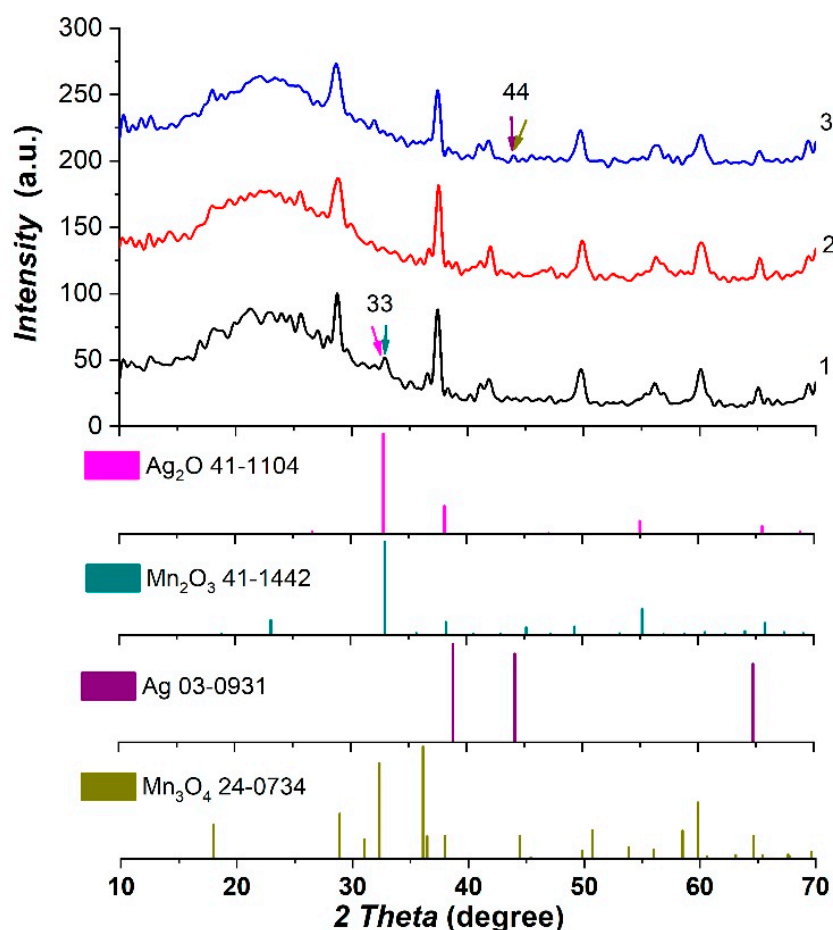
Figure 1. XRD patterns for prepared catalysts: 1—Ag/OMS-2, 2—Ag/0.05Fe–OMS-2, 3—Ag/0.1Fe–OMS-2.

A careful analysis of the diffraction pattern of the Ag/OMS-2 suggests a barely visible peak at 33° that can be indicative of some Ag_2O [45] or Mn_2O_3 phases. In addition, for the 0.1Fe–Ag/OMS-2 sample, a weak reflection at 44° is also observed, which may be associated with the presence of Ag^0 (JCDPS 03-0931). The absence of peaks ascribable to Fe and Ag phases suggests their high dispersion on the surface of manganese oxide, or their incorporation as cations into the OMS-2 structure. It is reported that the Fe addition improves the Ag dispersion in the Ag/Fe–MnO_x catalysts [2].

The XPS analysis data are summarized in Table 1 and Figure S2. Mn 3s and Mn 2p emissions were used to analyze the Mn oxidation state. For all investigated samples, the split of the Mn 3s component, arising from the coupling of the non-ionized 3s electron with the 3d valence band electron, is 4.3–4.5 eV, indicative mainly of MnO_2. Additionally, MnO_2, Mn_2O_3, and MnOOH are observed in the Mn 2p3/2 region after the curve fitting procedure according to Biesinger [46].

Table 1. XPS data for the prepared catalysts.

Sample	Ag/OMS-2	Ag/0.05Fe–OMS-2	Ag/0.1Fe–OMS-2
Mn 2p3/2	640.6	640.4	641.0
(eV)	641.6	641.5	641.9
Mn (III)/Mn(IV)	0.13	0.17	0.28
Fe 2p3/2 (eV)	–	711.0	711.0
Ag 3d5/2 (eV)	368.1	368.0	368.0
O1s-Lattice (eV)	529.7 (59%) *	529.6 (49%)	529.8 (66%)
O1s-OH (eV)	531.9 (41%)	532.2 (51%)	531.9 (34%)

* in parenthesis the relative percentage of this component with respect to total oxygen.

Table 1 shows that the relative amount of Mn(III) increases with the increasing iron content in the material. The binding energy of Fe 2p3/2 is 711 eV for all Fe-modified samples, and is consistent with the literature values for Fe^{3+} in Fe_2O_3 [47,48]. No hints of the presence of Fe^{2+} or Fe^{4+} are noticed [49].

For all samples, the Ag 3d 5/2 binding energy is centered at 368.0 eV, which is characteristic of metallic Ag [50,51]. Two types of oxygen species are observed on the surface of the Ag-containing catalysts (see Table 1 and Figure S2b). The O1s XPS peak at 529.6–529.8 eV, and a second peak with the BE of 532 eV, are observed. The first O1s peak is associated with the lattice oxygen ($O_{Lattice}$) in Mn–O–Mn. The O1s peak with the BE at 532 eV can be ascribed to the hydroxyl-like group (OH), e.g., H_2O adsorbed onto the surface [52]. Also, the region of 530–534 eV may be associated with either signals originating from lattice oxygen, hydroxyls, and water molecules, or, in most cases, organic contaminants containing oxygen atoms [53]. The highest OH content (51%) is found for the Ag/0.05Fe–OMS-2 catalyst, along with a positive shift in BE in comparison with the other two samples. It is reported in the literature that OH− groups play an important role in the oxidation of formate species to CO_2 and H_2O [2,54,55]. Also, a decrease in $O_{Lattice}$ content (49%), and a negative shift of the O1s BE from 529.7–8 eV to 529.6 eV, is observed for the Ag/0.05Fe–OMS-2 catalyst. It can be assumed that in the Ag/0.05Fe–OMS-2 catalyst, the electron transfer from Ag to $O_{Lattice}$ occurs through the Fe-embedded species, inducing the negative shift of the $O_{Lattice}$ peak, and may increase the amount of AgO_x species participating in selective ethanol oxidation. Similar behavior of Ag/Fe-MnO$_x$ catalysts was observed in Reference [2].

Table 2 shows the surface composition derived from the XPS analysis, which is compared with the elemental composition determined by XRF analysis listed in parenthesis. According to the XRF and XPS data, the amount of the introduced Fe modifier is close to the nominal amount, nevertheless, the amount of the surface iron is lower than the bulk one in the Ag/0.05Fe–OMS-2, and is slightly higher in Ag/0.1Fe–OMS-2. This finding is also reflected in the K/Mn ratio.

Table 2. Surface composition (XPS) and elemental composition (XRF) for the prepared samples.

Sample	K/Mn XPS (XRF)	Ag/Mn XPS (XRF)	Fe/Mn XPS (XRF)
Ag/OMS-2	0.14 (0.13)	0.10 (0.052)	–
Ag/0.05Fe–OMS-2	0.10 (0.13)	0.12 (0.056)	0.052 (0.054)
Ag/0.1Fe–OMS-2	0.04 (0.10)	0.08 (0.051)	0.125 (0.098)

The Fe introduction results in a decrease in the surface K concentration, as evidenced by the surface K/Mn ratio that is lower than the corresponding XRF value. This is more pronounced in the case of Ag/0.1Fe–OMS-2. Such a finding can be related to the partial K substitution by Fe cations on the surface of samples. A higher amount of iron leads to the enrichment of the surface, with a prevalent iron localization on the outer part of the channels.

On the contrary, the addition of Ag into the unmodified OMS-2 leads to the homogeneous K distribution on the surface and in the bulk of OMS-2, as evidenced by the K/Mn ratios obtained by XPS and XRF, which are close to each other.

According to the XPS results, the Ag content on the catalyst surface (Ag/Mn atomic ratio) decreases in the following order: Ag/0.05Fe–OMS-2 > Ag/OMS-2 > Ag/0.1Fe–OMS-2, which may be associated with silver distribution, as relatively large nanoparticles, on the surface of the Ag/0.1Fe–OMS-2 sample, in comparison with the Ag/0.05Fe–OMS-2 and Ag/OMS-2 samples. It is consistent with the XRD results, and the reflection related to Ag^0 species at the angle of ~44° is observed for Ag/0.1Fe–OMS-2 sample (Figure 1, blue curve).

The Ag/0.1Fe–OMS-2 is the sample with the lowest content of OH species, and features the highest ratio of Mn(III)/Mn(IV) (Table 1). This can be associated with the formation of nanoparticles of the separated Fe-containing phase, with the introduced Fe^{3+}

being partially embedded in the MnO$_2$ crystalline lattice. According to the XPS/XRF data (Table 2), the surface of this sample is enriched in Fe, and is depleted in Ag and K, as evidenced by the comparison of the XPS and XRF Fe/Mn, Ag/Mn, and K/Mn ratios. Low surface Ag concentration (Ag/Mn = 0.08) can be connected with its redistribution in the form of rather large metal particles. An electron density transfer from Ag^0 species to Mn^{4+} explains the high Mn(III)/Mn(IV) ratio for this sample. The Ag content is similar for the Ag/OMS-2 and Ag/0.1Fe–OMS-2 samples (XRF data in Table 2), while the Ag/Mn ratios taken from the XPS data are different.

The differences in the Ag content (XPS results in Table 2) in the samples prepared may be connected with the mechanism of Ag$^+$ interaction with the surfaces of the unmodified OMS-2 and Fe-containing samples at the stage of wet impregnation by the water solution of silver nitrate. The manganese oxide materials possess high ability to ion exchange with Ag cations, especially at low pH [56]. Silver can be uniformly distributed as small nanoparticles in the Ag/OMS-2 and Ag/0.05Fe–OMS-2 samples.

Due to the distribution of the Fe modifier as FeO$_x$ species on the 0.1Fe–OMS-2 catalyst surface (Figure 2), which leads to the changing of the surface composition of this sample, the sorption ability of the surface towards Ag$^+$ ions decreases. As a result, silver nitrate is deposited, with the formation of relatively large precursor particles on the surface of 0.1Fe–OMS-2. The precursor decomposes during the calcination stage, to yield metallic Ag nanoparticles. The appearance of the XRD reflection at ~44° in Figure 1 (blue curve) for this sample supports this conclusion. Similar behavior is observed earlier [57] for Ag-supported silica catalysts pre-calcined at different temperatures.
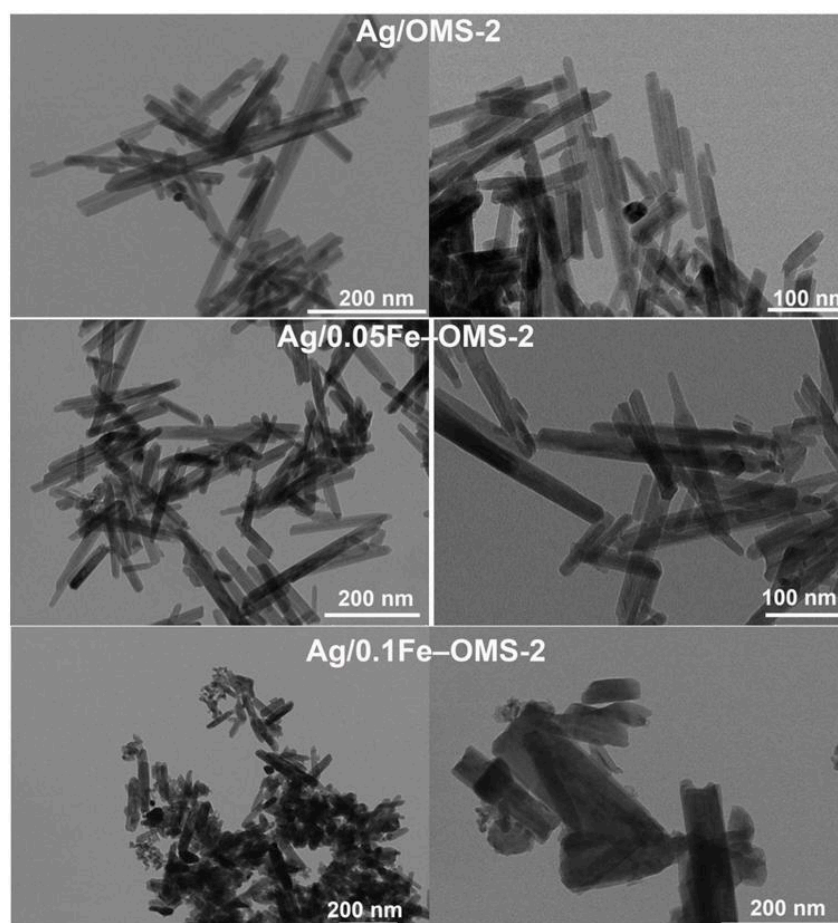

Figure 2. TEM images for investigated samples.

2.2. Study of Texture Properties and Morphology

Table 3 presents the textural characteristics for the prepared catalysts. The Ag/0.05Fe–OMS-2 sample features the largest surface area. Figure S3 presents the pore size distribution curves for the prepared Ag-containing samples. According to the calculation of the microporosity (t-plot), it is shown that the volume of micropores does not change after the addition of Ag. This fact allows for the exclusion of the decrease in the specific surface area, due to the clogging of the smaller pores by silver particles.

Table 3. Textural characteristics of the prepared catalysts.

Sample	S_{BET} (m^2/g)	Vp (cm^3/g)	dp (nm)
Ag/OMS-2	49	0.30	27.3
Ag/0.05Fe–OMS-2	41	0.27	26.9
Ag/0.1Fe–OMS-2	33	0.27	30.6

Figure S4 shows the morphology features for the prepared samples. The SEM images for the unmodified Ag/OMS = 2 sample show the needle-like particle characteristics of cryptomelane, which are aggregated into agglomerates with sizes of ~2–3 μm. At the same time, the SEM images for the Fe-modified samples obtained at comparable resolution show the predominant granular morphology. The Fe addition affects the stages of formation and subsequent growth of the OMS-2 crystals. The modifier cations adsorbed by the edges of the plane, along which the directed growth of nanorods occurs, suppress their further formation. This conclusion is confirmed by the TEM images presented in Figure 2.

2.3. H_2–TPR and TPO Results

It is known that the material reducibility can be significantly enhanced by loading noble metals [58]. The reduction profiles for the Ag-containing catalysts show the presence of the interaction between silver and manganese oxide favoring the hydrogen spillover from silver atoms to manganese oxides (Figure S5).

The spillover effect of adsorbed hydrogen from the Ag particles on the surface of oxide and the spillover of atomic oxygen from the oxide surface onto the Ag particle occur [59]. Previous studies report that the catalyst reducibility correlates with the concentration of oxygen vacancies, i.e., the catalysts with better reducibility (lower reduction temperature in the H_2–TPR experiment) could produce more oxygen vacancies [55,60]. The H_2–TPR profiles for the Ag-containing, Fe-modified catalysts differ from those for the Ag/OMS-2 sample, which may be associated with the interaction between the Ag- and Fe-containing species embedded in the MnO_x lattice (Figure S5). The Fe cations embedded into the MnO_x lattice, by replacing those of Mn, feature a fine distribution, thus, the Ag species located on the catalyst surface are close to both the Mn and Fe atoms. The contact between the Ag and Fe is claimed to be the main factor that differentiates $Ag/Fe–MnO_x$ from Ag/MnO_x.

All samples are characterized by the wide peak of several components in H_2–TPR profiles. Thus, for the Ag/OMS-2 sample, these are the maximum at 247 °C, attributed to the simultaneous reduction in manganese oxides [61], as well as two shoulders at temperatures of 170 and 350 °C. The low-temperature shoulder at 170 °C may also be due to the reduction in the adsorbed oxygen on the sample surface [62–64]. The shoulder at 350 °C may be due to the reduction in the manganese oxide that is not in contact with silver. On the other hand, the authors of Ref. [64], who studied the reduction in Ag (1–10 wt.%)/TiO_2 catalysts, attributed the peak in the temperature range of 348–384 °C to the reduction in silver (I) oxide. In their opinion, additional reduction peaks can be due to the reduction in pore-deposited Ag_2O, in which bulk lattice oxygen species experience a greater extent of the support interactions. The profiles for the Ag/0.05Fe–OMS-2 and Ag/0.1Fe–OMS-2 samples exhibit the peaks at temperatures of 254 and 269 °C, and the shoulders at 314 and 345 °C, respectively. The main peak has a complex structure similar to the unmodified Ag/OMS-2. It can be assumed that some of the components belong to the reduction in the

manganese oxides, along with the contribution from the reduction in iron species [65,66]. It is noteworthy that neither the presence of Fe or Ag has an effect on the high-temperature reduction stage, and the maxima in the range of 680–700 °C, attributed to the reduction in Mn_3O_4/MnO_2 oxides to MnO, do not change their positions.

Table S1 shows the amounts of H_2 consumed by the prepared catalysts. The presence of Fe changes the distribution of Ag species in the Ag/0.05Fe–OMS-2 sample and their state. XPS data show that the addition of 5 mol.% Fe increases the content of adsorbed O and/or OH groups (51% in comparison with 41% and 34% for other samples), and/or oxygen vacancy on the surface and their BE, and decreases the $O_{Lattice}$ content. The distribution of Ag as small nanoparticles seems to help achieve the maximal amount of H_2 consumption (0.060 mmol H_2/g), according to the H_2–TPR data for Ag/0.05Fe–OMS-2., i.e., the highest amount of the adsorbed oxygen on the sample surface. This may be associated with the cooperative action between the Ag-containing and Fe-containing species embedded into the OMS-2 surface.

Figure S6 shows the TPO profiles. The behavior of the TPO profiles for the Ag-containing samples is characterized by the presence of a single reoxidation peak: these are the TPO peaks at 226, 260, and 329 °C for Ag/OMS-2, Ag/0.1Fe–OMS-2, and Ag/0.05Fe–OMS-2, respectively. In comparison with the Ag/0.05Fe–OMS-2, the Ag/0.1Fe–OMS-2 sample features the maximal amount of $O_{Lattice}$ species, and the highest value of the Mn(III)/Mn(IV) ratio. The highest Mn(III) concentration on the sample surface explains the efficient activation of the gas-phase oxygen during the catalyst reoxidation (Figure S6).

In the Ag/0.05Fe–OMS-2 sample, the Ag contact with the oxygen of the manganese oxide crystal lattice occurs indirectly, through the highly distributed iron-containing species, leading to a relatively low activation of the gas-phase oxygen in the TPO mode (Figure S6). In contrast to this, Ag/0.1Fe–OMS-2 seems to have smaller number of Ag particles, which are in contact with the Fe-containing species, due to the large size of the latter (Figure 2). On the other hand, the increase in $O_{surf}/(O_{surf} + O_{latt})$ and $Ag^+/(Ag^0 + Ag^+)$ occurs simultaneously after the Fe doping of the Ag-containing OMS-2 catalyst in comparison with pristine Ag/OMS-2 catalyst. Hence, the high amount of O-containing species for Ag/0.05Fe–OMS-2 (Table 1) may be responsible for the high catalytic activity of this sample (Table 4). In addition, it can be seen from the XPS data that the silver content on the surface increases in the following order: Ag/0.05Fe–OMS-2 > Ag/OMS-2 > Ag/0.1Fe–OMS-2 (Table 2). The same order is observed for the amount of hydrogen consumed in the H_2–TPR mode (Table S1). The higher surface silver-loading can also play a major role in the catalyst activity.

Table 4. Catalytic data for prepared catalysts in selective ethanol oxidation (GHSV = 7200 mL g^{-1} h^{-1}, Et/O_2 = 2/18).

Sample	T_{50} (°C)	S_{Ac50} (%)	T_{80} (°C)	S_{Ac80} (%)	S_{CO280} (%)
Ag/OMS-2	131	97	150	93	5.0
Ag/0.05Fe–OMS-2	135	96	155	93	3.6
Ag/0.1Fe–OMS-2	166	93	190	82	9.2
OMS-2 [67]	132	87	152	69	17

S_{Ac50}, S_{Ac80} ($S_{CO_2 80}$) are acetaldehyde (CO_2) selectivity at 50% and 80% of ethanol conversion, respectively (formation of small amounts of methyl and ethyl acetate is also observed).

2.4. Catalytic Properties of the Ag-Containing Catalysts

The catalytic properties of the prepared samples were studied in selective oxidation of ethanol (Figures 3 and 4).
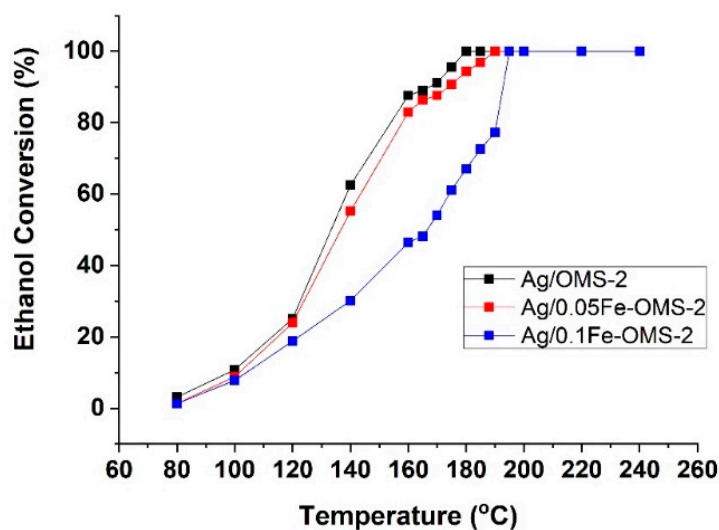
Figure 3. Temperature dependences of ethanol conversion for prepared samples. Reaction conditions: GHSV = 7200 mL g^{-1} h^{-1}, Et/O$_2$ = 2/18.
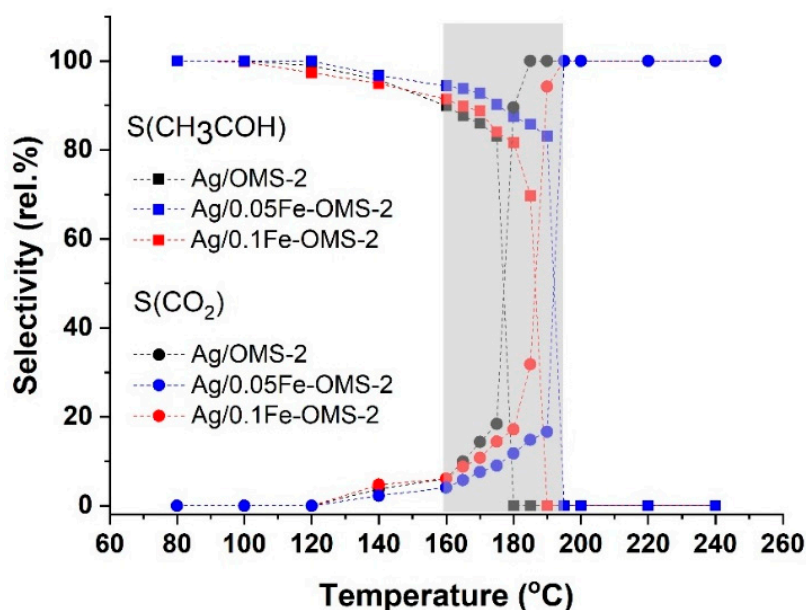

Figure 4. Temperature dependences of acetaldehyde and CO$_2$ selectiveness for prepared samples. Reaction conditions: GHSV = 7200 mL g^{-1} h^{-1}, Et/O$_2$ = 2/18.

Temperatures of 50% and 80% ethanol conversion decrease in the following order: Ag/0.1Fe–OMS-2 < Ag/0.05Fe–OMS-2 ≤ Ag/OMS-2. Thus, the increase in the iron content leads to a decrease in the activity of the investigated catalysts in the ethanol oxidation process (Figure 3, Table 4).

The catalytic data also indicate that part of the Fe$_2$O$_3$ impurity located on the external surface of the anisotropic OMS-2 crystals in the Ag/0.1Fe–OMS-2 sample is in contact with the supported Ag species. It is shown that oxygen can hardly be transferred from Fe$_2$O$_3$ to Ag [29]. This is because the formation of surface oxygen vacancies (the rate-determining step for oxygen reverse spillover) is relatively difficult in Fe$_2$O$_3$ [68–70]. This reverse spillover is also energetically unfavorable: ΔH (Ag$_2$O) = −31.1 kJ/mol, which is more than 26 times smaller than that of Fe$_2$O$_3$ (ΔH = −824.2 kJ/mol). As a result, Wang et al. claimed [29] that Ag particles can hardly improve the oxygen utilization and O$_x^-$ generation using an Ag/Fe$_2$O$_3$ catalyst prepared by impregnation. Thus, they show that the most active catalyst in soot oxidation is the one that contains a layer of CeO$_2$

nanoparticles between the Ag and Fe_2O_3 particles. The Ag-loading facilitates both the utilization of ceria bulk oxygen and the activation of gaseous O_2. On the other hand, An et al. [71] found that the low-temperature activity of Pt/Fe_2O_3 catalyst may be assigned to the appearance of suitable interactions between the Pt particles and iron oxide supports (Pt–O–Fe). Through this interaction, highly dispersed Pt can weaken the Fe–O bond at the Pt/FeO_x interface, thus, increasing the mobility of the active oxygen involved in HCHO oxidation. The catalytic properties of the prepared samples were compared with different Mn-based catalysts in selective oxidation of ethanol (Table 5).

Table 5. The comparison of catalytic properties of different catalysts in the ethanol oxidation.

Catalyst	Ethanol/O_2 (vol./vol)	SV (ml/g_{cat}/h)	T_{50} (°C)	S_{Ac50} (%)	T_{80} (°C)	S_{Ac80} (%)	Ref.
K–OMS-2	1/1	100,000	190	100	220	82	[24]
OMS-2	2/18	7200	132	87	152	69	[67]
Fe–γ-MnO_2 (M/Mn = 1/9)	1/1	100,000	185	97	220	90	[72]
Fe–OMS-2 (M/Mn = 1/30)	1/1	100,000	180	95	212	65	[72]
Ag/OMS-2 (5 wt.% Ag)	2/18	7200	131	97	150	93	This work
Ag-hollandite nanofibers $AgMnO_4/Mn(NO_3)_2$ = 2/3	5/10	36,000	220	90	235	80	[73]
Ag/Fe–OMS-2 (Mn/Fe = 1/20, 5 wt.% Ag)	2/18	7200	135	96	155	93	This work
Ag/Fe–OMS-2 (Mn/Fe = 1/10, 5 wt.% Ag)	2/18	7200	166	93	190	82	This work
Au/Fe–OMS-2 (1 wt.% Au)	2.5/2.5	100,000	–	–	200	65	[74]
V_2O_5–TiO_2	2/18	3600 1/h	110	60 *	130	80 *	[75]

* yields.

The selectivity towards acetaldehyde in the 50% ethanol conversion increases in the following order: Ag/0.1Fe–OMS-2 < Ag/0.05Fe–OMS-2 ≤ Ag/OMS-2 (Figure 4) In the 80% ethanol conversion, the selectivity towards acetaldehyde formation slightly decreases for Ag/OMS-2 and the Ag/0.05Fe–OMS-2 catalyst, and is 93%. For the catalyst containing 1 mol.% Fe, the acetaldehyde selectivity drops to 82% at T_{80}. The CO_2 selectivity at temperature of 80% conversion is the highest for Ag/0.1Fe–OMS-2, while the TPO temperature is lower, and the Mn(III)/Mn(IV) ratio is higher than for Ag/0.05Fe–OMS-2. Hindered oxygen transfer from FeO_x impurities to Ag, and strong FeO_x–ethanol bonding, may play a crucial role in selective ethanol oxidation, and enhances the total oxidation process. Moreover, the lowest activation of the gas-phase oxygen in the TPO experiment (Ag/0.05Fe–OMS-2) reveals the stronger bonding of Ag- and Fe-containing species with manganese; it is likely that Ag contacts with the oxygen of the manganese oxide crystal lattice through the iron-containing species. It is well-known that a stronger interaction of oxygen with the catalyst surface is more preferable for selective oxidation. Thus, despite the slightly higher activity of Ag/OMS-2, the CO_2 selectivity (S_{CO280}) is higher (5.0%) in comparison with Ag/0.05Fe–OMS-2 (3.6%).

According to our previous study [67], we can claim that Ag addition into pure OMS-2 does not influence ethanol conversion (Figure S7a), and improves acetaldehyde selectivity (Figure S8). Figure S7 shows that ethanol conversion decreases in the following order: OMS-2 > Ag/OMS-2 > Ag/0.05Fe–OMS-2 ≥ 0.1Fe–OMS-2. Thus, active Ox species do not bond with any additivities, and labile surface oxygen can easily migrate from catalyst surface to organic molecules to oxidize them. Doping OMS-2 with iron and/or silver obviously reduces this ability. As expected, the presence of FeO_x species does not prevent mobility of oxygen species, due to its high volumetric oxygen consumption. However, Figure S8 shows that acetaldehyde selectivity decreases in the following range: Ag/0.05Fe–OMS-2 > 0.05Fe–OMS-2 ≥ Ag/0.1Fe–OMS-2. The starting temperature of sharp growth of CO_2 selectivity for OMS-2 and 0.1Fe–OMS-2 is 160 °C, while for the 5 mol.% Fe-containing silver catalyst, this parameter raises up to 190 °C. Thus, the FeO_x–ethanol interaction contributes to the selectivity of the target product. In case of Ag/0.1Fe–OMS-2

FeO_x species bond both with Ag and surface reactants, and the interaction is weaker, which leads to a higher acetaldehyde selectivity in comparison with 0.1Fe–OMS-2. However, the transfer of oxygen and O_x^- generation in Ag/FeO_x is difficult, and the best selectivity is obtained for the catalyst highly dispersed iron on its surface—Ag/0.05Fe–OMS-2. Therefore, the addition of highly dispersed iron (only 5 mol.% in this investigation), and the introduction of 5 mass.% of Ag into OMS-2, makes it possible to perform the ethanol oxidation process with a high selectivity toward acetaldehyde in a wide temperature range.

3. Materials and Methods

The manganese oxide catalysts with the OMS-2 structure were prepared by hydrothermal synthesis [13]. To prepare the iron-modified OMS-2 with a molar ratio of Fe/Mn = 0.05 and 0.1, the required amounts of aqueous iron nitrate ($Fe(NO_3)_3 \times 9H_2O$) were added to the initial $MnSO_4$ solution prior to mixing with the $KMnO_4$ solution. A precipitate was obtained by a redox reaction between the $MnSO_4$ and $KmnO_4$ ($Mn^{7+}/Mn^{2+} = 1/1$ molar ratio) solutions, at a pH of 1. The hydrothermal treatment was carried out at 120 °C for 24 h, followed by filtration and washing with distilled water up to a pH of 7. Finally, the samples were thermally treated at 450 °C for 2 h. Ag was then added by the incipient wetness impregnation method. Samples of OMS-2, 0.05Fe–OMS-2, and 0.1Fe–OMS-2 were impregnated with silver nitrate solution (chemically pure) of the required concentration. Then samples were kept at room temperature for 30 min at a constant stirring, dried at 120 °C, and, finally, thermally treated at 450 °C for 1 h. The theoretical Ag-loading was 5 wt.%.

Textural characteristics of the prepared catalysts were investigated using the low temperature nitrogen sorption (TriStar II 3020 and 3 Flex analyzers, Micromeritics, Norcross, GA, USA). The morphology of the samples was studied on the TESCAN VEGA 3 SBH scanning electron microscope (Tescan, Brno, Czech Republic) and a CM-12 Philips transmission electron microscope (Philips, Eindhoven, The Netherlands).

To identify the catalyst phase compositions, the diffractometer XRD-6000 (Shimadzu, Kyoto, Japan) with a monochromatized Cu Kα radiation (λ = 1.5418 Å) and PCPDFWIN database were used. The elemental composition was examined using the X-ray fluorescence wavelength-dispersive sequential spectrometer XRF-1800 (Shimadzu, Kyoto, Japan).

The X-ray photoelectron spectroscopy (XPS) analysis of the powders was carried out using a VG Microtech ESCA 3000 Multilab (VG Scientific, Sussex, UK), with an Al Kα source (1486.6 eV) run at 14 kV and 15 mA in constant analyser energy (CAE) mode. For the individual peak energy regions, pass energy of 20 eV, set across the hemispheres, was used. The constant charging of the samples was removed by referencing all the energies to the C 1 s peak energy set at 285.1 eV, arising from adventitious carbon. The XPS data were examined using the CASA XPS software (version 2.3.17, Casa Software Ltd. Wilmslow, Cheshire, UK, 2009). For the peak shape, a Gaussian (70%)–Lorentzian (30%) line shape, defined in Casa XPS as GL (30) profiles, was used for each component of the main peaks, after a Shirley background subtraction. The binding energy values were quoted with a precision of ±0.15 eV, and the atomic percentage with a precision of ±10%.

The temperature-programmed reduction method was used to determine the reaction ability of the prepared samples towards H_2 (H_2–TPR) using the chemisorption analyzer ChemiSorb 2750 (Micromeritics, Norcross, GA, USA). The H_2-containing flow (10 vol. %.) was used as a reaction mixture for H_2–TPR. The temperature was increased from 25 to 800 °C at a heating rate of 10 °C/min for the TPR experiments.

The reoxidation of the samples using the temperature-programmed oxidation (TPO) was carried out after TPR–H_2 using the chemisorption analyzer ChemiSorb 2750 (Micromeritics, Norcross, GA, USA). The temperature was increased from 25 to 700 °C (10 °C/min) in a flow of gas mixture 5 vol. % O_2, at a flow rate of 20 mL/min.

Catalytic properties were studied in the U-type fixed-bed reactor with i.d. of 6 mm. The temperature was increased from 25 to up to 240 °C with steps of 15–20 °C. The flow composition of 2 vol. % C_2H_5OH, 18 vol. % O_2, and He for balance was fed with the WHSV

of 7200 mL g^{-1} h^{-1}. The composition of the flows of reagents and products was analyzed using online gas chromatograph.

4. Conclusions

The catalysts prepared in this work were manganese oxides with an octahedral molecular sieve structure. For the low-loading, Fe-modified sample, the modifier is distributed between the surface and the bulk, while the Ag/0.1Fe–OMS-2 sample features some segregated iron on the surface. The Ag addition to OMS-2 leads to the homogeneous distribution of K and Ag on the surface and in the bulk of OMS-2.

The reduction profiles for the Ag-containing catalysts show the presence of the interaction between silver and manganese oxide that favors the hydrogen spillover from silver atoms to manganese oxides. The XPS data show that the adsorbed oxygen content on the catalyst surface decreases in the following order: Ag/0.05Fe–OMS-2 > Ag/OMS-2 > Ag/0.1Fe–OMS-2.

The strong interaction of the metal silver nanoparticles with manganese oxide is confirmed by the growth of the Mn(III)/Mn(IV) ratio for the Ag/0.1Fe–OMS-2 sample. It can be assumed that in the sample containing a higher amount of iron, in addition to the silver interaction with manganese oxide, there also exists an interaction between the silver and the isolated FeO$_x$ species. It is likely that in the Ag/0.1Fe–OMS-2 sample, the Ag contact with the lattice oxygen of manganese does not occur directly, but through iron oxide, which leads to a more efficient activation of gas-phase oxygen during its reoxidation. However, higher silver content, according to the XPS data, in the Ag/0.05Fe–OMS-2 sample seems to play the major role in its low-temperature activity in ethanol oxidation to acetaldehyde. This may be achieved by a good dispersion of iron and silver within the OMS-2 structure. Thus, the catalyst with highly dispersed iron and silver species is expected to have high activity and selectivity towards acetaldehyde in the ethanol oxidation reaction. The interaction between the FeO$_x$ isolated species formed on the OMS-2 surface with silver improves the reoxidation of manganese oxides, but decreases the O$_x$– generation and oxygen transfer to Ag in the Ag/0.1Fe–OMS-2 catalyst prepared by impregnation. This, therefore, decreases the catalyst activity and selectivity towards acetaldehyde.

Thus, the synergetic effect is observed, but the balance required in the catalytic activity is found to be greatly influenced by the Mn/Fe ratio in the mixed oxide that is formed. According to our results, we manage to achieve it in the case of Ag/0.05Fe–OMS-2. Thus, the introduction of 5 mol.% Fe into the manganese dioxide with the OMS-2 structure makes it possible to obtain the catalyst in which iron species are highly dispersed, and the formation of individual oxide iron phases on the surface does not occur. In addition, the subsequent silver deposition by the incipient wetness impregnation on the 0.05Fe–OMS-2 results in a sample with a high content of adsorbed oxygen species on the surface, which apparently plays an important role, since the Ag introduction into OMS-2 and 0.05Fe–OMS-2 results in the preparation of catalysts with similarly high levels of activity (T$_{80}$ = 150–155 °C) selectivity (S$_{Ac80}$ = 93%) towards the acetaldehyde formation. Further investigation will focus on stability experiments to reveal the role of highly dispersed iron species on the stability of catalysts in selective ethanol oxidation.

Supplementary Materials: The following supporting information can be downloaded at: https://www.mdpi.com/article/10.3390/catal12080872/s1, Figure S1: XRD patterns for prepared catalysts; Figure S2: XPS regions (a) Mn2p and (b) O1s; Figure S3: Texture characteristics for prepared samples; Figure S4: TEM images for investigated samples; Figure S5: H$_2$–TPR profiles for prepared samples; Figure S6: TPO profiles for prepared samples; Figure S7: Light-off curves for catalysts with and without Ag [67]. Reaction conditions: GHSV = 7200 mL g^{-1} h^{-1}, Et/O$_2$ = 2/18; Figure S8: Temperature dependences of acetaldehyde and CO$_2$ selectivity for catalysts with and without Ag [67]. Reaction conditions: GHSV = 7200 mL g^{-1} h^{-1}, Et/O$_2$ = 2/18; Table S1: H$_2$ consumption during H$_2$–TPR experiments performed on the investigated catalysts before and after Ag introduction.

References

1. Assal, M.; Shaik, M.R.; Kuniyil, M.; Khan, M.; Kumar, J.V.S.; Alzahrani, A.Y.; Al-Warthan, A.; Al-Tamrah, S.A.; Siddiqui, M.R.H.; Hashmi, S.A.; et al. Silver-doped manganese based nanocomposites for aerial oxidation of alcohols. *Mater. Express* **2018**, *8*, 35–54. [CrossRef]
2. Li, D.; Yang, G.; Li, P.; Wang, J.; Zhang, P. Promotion of formaldehyde oxidation over Ag catalyst by Fe doped MnO$_x$ support at room temperature. *Catal. Today* **2016**, *277*, 257–265. [CrossRef]
3. Ochoa, J.V.; Cavani, F. Gas-Phase Oxidation of Alcohols: Innovation in Industrial Technologies and Recent Developments. *RSC Green Chem.* **2015**, *28*, 203–230. [CrossRef]
4. Kaichev, V.V.; Chesalov, Y.A.; Saraev, A.A.; Klyushin, A.Y.; Knop-Gericke, A.; Andrushkevich, T.V.; Bukhtiyarov, V.I. Redox mechanism for selective oxidation of ethanol over monolayer V$_2$O$_5$/TiO$_2$ catalysts. *J. Catal.* **2016**, *338*, 82–93. [CrossRef]
5. Liu, P.; Hensen, E.J.M. Highly Efficient and Robust Au/MgCuCr$_2$O$_4$ Catalyst for Gas-Phase Oxidation of Ethanol to Acetaldehyde. *J. Am. Chem. Soc.* **2013**, *135*, 14032–14035. [CrossRef] [PubMed]
6. Wang, P.; Luo, H.; Wang, J.; Han, B.; Mei, F.; Liu, P. Synergistic effect between gold nanoparticles and Fe-doped γ-MnO$_2$ toward enhanced aerobic selective oxidation of ethanol. *Catal. Sci. Technol.* **2020**, *10*, 4332–4339. [CrossRef]
7. Grabchenko, M.V.; Mamontov, G.V.; Zaikovskii, V.I.; La Parola, V.; Liotta, L.F.; Vodyankina, O.V. Design of Ag-CeO$_2$/SiO$_2$ catalyst for oxidative dehydrogenation of ethanol: Control of Ag–CeO$_2$ interfacial interaction. *Catal. Today* **2019**, *333*, 2–9. [CrossRef]
8. Vodyankina, O.V.; Blokhina, A.S.; Kurzina, I.A.; Sobolev, V.I.; Koltunov, K.Y.; Chukhlomina, L.N.; Dvilis, E.S. Selective oxidation of alcohols over Ag-containing Si$_3$N$_4$ catalysts. *Catal. Today* **2013**, *203*, 127–132. [CrossRef]
9. Son, Y.C.; Makwana, V.D.; Howell, A.R.; Suib, S.L. Efficient, Catalytic, Aerobic Oxidation of Alcohols with Octahedral Molecular Sieves. *Angew. Chem. Int. Ed.* **2001**, *40*, 4280–4283. [CrossRef]
10. Jia, X.; Ma, J.; Xia, F.; Gao, J.; Xu, J. Switching acidity on manganese oxide catalyst with acetylacetones for selectivity-tunable amines oxidation. *Nat. Commun.* **2019**, *10*, 2338. [CrossRef]
11. Elmaci, G.; Erturk, A.S.; Sevim, M.; Metin, O. MnO$_2$ nanowires anchored on mesoporous graphitic carbon nitride (MnO$_2$@mpg-C$_3$N$_4$) as a highly efficient electrocatalyst for the oxygen evolution reaction. *Int. J. Hydrogen Energy* **2019**, *44*, 17995–18006. [CrossRef]
12. Elmaci, G.; Cerci, S.; Sunar-Cerci, D. The evaluation of the long-term stability of α-MnO$_2$ based OER electrocatalyst in neutral medium by using data processing approach. *J. Mol. Struct.* **2019**, *1195*, 632–640. [CrossRef]
13. de Guzman, R.N.; Shen, Y.-F.; Neth, E.J.; Suib, S.L.; O'Young, C.L.; Levine, J.M.; Newsam, S. Synthesis and Characterization of Octahedral Molecular Sieves (OMS-2) Having the Hollandite Structure. *Chem. Mater.* **1994**, *6*, 815–821. [CrossRef]
14. Rasul, S.; Suzuki, S.; Yamaguchi, S.; Miyayama, M. Manganese oxide octahedral molecular sieves as insertion electrodes for rechargeable Mg batteries. *Electrochim. Acta* **2013**, *110*, 247–252. [CrossRef]
15. Jiang, C.H.; Dou, S.X.; Liu, H.K.; Ichihara, M.; Zhou, H.S. Synthesis of spinel LiMn$_2$O$_4$ nanoparticles through one-step hydrothermal reaction. *J. Power Sources* **2007**, *172*, 410–415. [CrossRef]
16. Lee, S.W.; Kim, J.; Chen, S.; Hammond, P.T.; Shao-Horn, Y. Carbon Nanotube/Manganese Oxide Ultrathin Film Electrodes for Electrochemical Capacitors. *ACS Nano* **2010**, *4*, 3889–3896. [CrossRef]
17. Zhang, L.L.; Tu, J.J.; Lyu, L.; Hu, C. Enhanced catalytic degradation of ciprofloxacin over Ce-doped OMS-2 microspheres. *Appl. Catal. B* **2016**, *181*, 561–569. [CrossRef]
18. Huang, Y.; Yan, J.; Zhang, N.; Zheng, K.; Hu, Y.; Liu, X.; Meng, X. The Effect of Metal Ions as Dopants on OMS-2 in the Catalytic Degradation. *Catal. Lett.* **2020**, *150*, 2021–2026. [CrossRef]
19. Deng, H.; Kang, S.; Ma, J.; Zhang, C.; He, H. Silver incorporated into cryptomelane-type Manganese oxide boosts the catalytic oxidation of benzene. *Appl. Catal. B* **2018**, *239*, 214–222. [CrossRef]

20. He, B.; Cheng, G.; Zhao, S.; Zeng, X.; Li, Y.; Yang, R.; Sun, M.; Yu, L. Controlled synthesis of tunnel-structured MnO_2 through hydrothermal transformation of δ-MnO_2 and their catalytic combustion of dimethyl ether. *J. Sol. State Chem.* **2019**, *269*, 305–311. [CrossRef]

21. Sun, M.; Li, W.; Zhang, B.; Cheng, G.; Lan, B.; Ye, F.; Zheng, Y.; Cheng, X.; Yu, L. Enhanced catalytic performance by oxygen vacancy and active interface originated from facile reduction of OMS-2. *Chem. Eng. J.* **2018**, *331*, 626–635. [CrossRef]

22. Özacara, M.; Poyraz, A.S.; Genuino, H.C.; Kuo, C.-H.; Meng, Y.; Sui, S.L. Influence of silver on the catalytic properties of the cryptomelane and Ag-hollandite types manganese oxides OMS-2 in the low-temperature CO oxidation. *Appl. Catal. A* **2013**, *462–463*, 64–74. [CrossRef]

23. Ma, J.; Wang, C.; He, H. Transition metal doped cryptomelane-type manganese oxide catalysts for ozone decomposition. *Appl. Catal. B* **2017**, *201*, 503–510. [CrossRef]

24. Liu, P.; Duan, J.; Ye, Q.; Mei, F.; Shu, Z.; Chen, H. Promoting effect of unreducible metal doping on OMS-2 catalysts for gas-phase selective oxidation of ethanol. *J. Catal.* **2018**, *367*, 115–125. [CrossRef]

25. Dutov, V.V.; Mamontov, G.V.; Sobolev, V.I.; Vodyankina, O.V. Silica-supported silver-containing OMS-2 catalysts for ethanol oxidative dehydrogenation. *Catal. Today* **2016**, *278*, 164–173. [CrossRef]

26. Zhou, H.; Wang, J.Y.; Chen, X.; O'Young, C.L.; Sib, S.L. Studies of oxidative dehydrogenation of ethanol over manganese oxide octahedral molecular sieve catalysts. *Microporous Mesoporous Mater.* **1998**, *21*, 315–324. [CrossRef]

27. Shen, X.; Morey, A.M.; Liu, J.; Ding, Y.; Cai, J.; Durand, J.; Wang, Q.; Wen, W.; Hines, W.A.; Hanson, J.C.; et al. Characterization of the Fe-Doped Mixed-Valent Tunnel Structure Manganese Oxide KOMS-2. *J. Phys. Chem. C* **2011**, *115*, 21610–21619. [CrossRef]

28. Sun, M.; Yu, L.; Ye, F.; Diao, G.; Yu, Q.; Hao, Z.; Zheng, Y.; Yuan, L. Transition metal doped cryptomelane-type manganese oxide for low-temperature catalytic combustion of dimethyl ether. *Chem. Eng. J.* **2013**, *220*, 320–327. [CrossRef]

29. Wang, H.; Jin, B.; Wang, H.; Ma, N.; Liu, W.; Weng, D.; Wu, X.; Liu, S. Study of Ag promoted Fe_2O_3@CeO_2 as superior soot oxidation catalysts: The role of Fe_2O_3 crystal plane and tandem oxygen delivery. *Appl. Cat. B* **2018**, *237*, 251–262. [CrossRef]

30. Durán, F.G.; Barbero, B.P.; Cadús, L.E.; Rojas, C.; Centeno, M.A.; Odriozola, J.A. Manganese and iron oxides as combustion catalysts of volatile organic compounds. *Appl. Cat. B* **2009**, *92*, 194–201. [CrossRef]

31. Sun, W.; Li, X.; Zhao, Q.; Mu, J.; Chen, J. Fe–Mn Mixed Oxide Catalysts Synthesized by One-Step Urea-Precipitation Method for the Selective Catalytic Reduction of NO_x with NH_3 at Low Temperatures. *Catal. Lett.* **2018**, *148*, 227–234. [CrossRef]

32. Vodyankina, O.V.; Mamontov, G.V.; Dutov, V.V.; Kharlamova, T.S.; Salaev, M.A. Ag-containing nanomaterials in heterogeneous catalysis: Advances and recent trends. In *Advanced Nanomaterials for Catalysis and Energy*, 1st ed.; Sadykov, V.A., Ed.; Elsevier: Amsterdam, The Netherlands, 2019; Chapter 5; pp. 143–175. [CrossRef]

33. Shannon, R.D. Revised effective ionic radii and systematic studies of interatomic distances in halides and chalcogenides. *Acta Crystallogr.* **1976**, *32*, 751–767. [CrossRef]

34. Dey, S.; Dhal, G.C.; Mohan, D.; Prasad, R. Synthesis of silver promoted $CuMnO_x$ catalyst for ambient temperature oxidation of carbon monoxide. *J. Sci. Adv. Mater. Devices* **2019**, *4*, 47–56. [CrossRef]

35. Dutov, V.V.; Mamontov, G.V.; Zaikovskii, V.I.; Liotta, L.F.; Vodyankina, O.V. Low-temperature CO oxidation over Ag/SiO_2 catalysts: Effect of OH/Ag ratio. *Appl. Catal. B* **2018**, *221*, 598–609. [CrossRef]

36. Chen, D.; Qu, Z.; Sun, Y.; Gao, K.; Wang, Y. Identification of reaction intermediates and mechanism responsible for highly active HCHO oxidation on Ag/MCM-41 catalysts. *Appl. Catal. B* **2013**, *142–143*, 838–848. [CrossRef]

37. Kharlamova, T.; Mamontov, G.; Salaev, M.; Zaikovskii, V.; Popova, G.; Sobolev, V.; Knyazev, A.; Vodyankina, O. Silica-supported silver catalysts modified by cerium/manganese oxides for total oxidation of formaldehyde. *Appl. Catal. A* **2013**, *467*, 519–529. [CrossRef]

38. Ye, Q.; Zhao, J.; Huo, F.; Wang, J.; Cheng, S.; Kang, T.; Dai, H. Nanosized Ag/α-MnO_2 catalysts highly active for the low-temperature oxidation of carbon monoxide and benzene. *Catal. Today* **2011**, *175*, 603–609. [CrossRef]

39. Montaña, M.; Aparicio, M.S.L.; Ocsachoque, M.A.; Navas, M.B.; Barros, I.C.L.; Rodriguez-Castellón, E.; Casella, M.L.; Lick, I.D. Zirconia-Supported Silver Nanoparticles for the Catalytic Combustion of Pollutants Originating from Mobile Sources. *Catalysts* **2019**, *9*, 297. [CrossRef]

40. Chen, J.; Li, J.; Liu, Q.; Huang, X.; Shen, W. Chin Facile Synthesis of Ag-Hollandite Nanofibers and Their Catalytic Activity for Ethanol Selective Oxidation. *J. Catal.* **2007**, *28*, 1034–1036. [CrossRef]

41. Khan, I.A.; Sajid, N.; Badshah, A.; Wattoo, M.H.S.; Anjum, D.H. CO Oxidation Catalyzed by Ag Nanoparticles Supported on SnO/CeO_2. *Chem. Soc.* **2015**, *26*, 695–704. [CrossRef]

42. Dong, X.-Y.; Gao, Z.-W.; Yang, K.-F.; Zhang, W.-Q.; Xu, L.-W. Nanosilver as a new generation of silver catalysts in organic transformations for efficient synthesis of fine chemicals. *Catal. Sci. Technol.* **2015**, *5*, 2554–2574. [CrossRef]

43. Wen, C.; Yin, A.; Dai, W.-L. Recent advances in silver-based heterogeneous catalysts for green chemistry processes. *Appl. Catal. B* **2014**, *160–161*, 730–741. [CrossRef]

44. Ho, P.H.; Lee, S.C.; Kim, J.; Lee, D.; Woo, H.C. Properties of a manganese oxide octahedral molecular sieve (OMS-2) for adsorptive desulfurization of fuel gas for fuel cell applications. *Fuel Process. Technol.* **2015**, *131*, 238–246. [CrossRef]

45. Munoz-Rojas, D.; Oro-Sole, J.; Ayyad, O.; Gómez-Romero, P. Shaping hybrid nanostructures with polymer matrices: The formation mechanism of silver–polypyrrole core/shell nanostructures. *J. Mater. Chem.* **2011**, *21*, 2078–2086. [CrossRef]

46. Biesinger, M.C.; Payne, B.P.; Grosvenor, A.P.; Lau, L.W.M.; Gerson, A.R.; Smart, R.S.C. Resolving surface chemical states in XPS analysis of first row transition metals, oxides and hydroxides: Cr, Mn, Fe, Co and Ni. *Appl. Surf. Sci.* **2011**, *257*, 2717–2730. [CrossRef]

47. Yamashita, T.; Hayes, P. Analysis of XPS spectra of Fe^{2+} and Fe^{3+} ions in oxide materials. *Appl. Surf. Sci.* **2008**, *254*, 2441–2449. [CrossRef]

48. Makimizu, Y.; Nguyen, N.T.; Ahn, H.-J.; Yoo, J.E.; Hwang, I.; Kmentcand, S.; Schmuki, P.J. Effects of low oxygen annealing on the photoelectrochemical water splitting properties of α-Fe_2O_3. *Mater. Chem. A* **2020**, *8*, 1315–1325. [CrossRef]

49. Flak, D.; Chen, Q.; Mun, B.S.; Liu, Z.; Rękas, M.; Braun, A. In situ ambient pressure XPS observation of surface chemistry and electronic structure of α-Fe_2O_3 and γ-Fe_2O_3 nanoparticles. *Appl. Surf. Sci.* **2018**, *455*, 1019–1028. [CrossRef]

50. Santos, L.M.; Machado, W.A.; France, M.D.; Borges, K.A.; Paniago, R.M.; Patrocino, A.O.T.; Machado, A.E.H. Structural characterization of Ag-doped TiO_2 with enhanced photocatalytic activity. *RSC Adv.* **2015**, *5*, 103752–103759. [CrossRef]

51. Ren, H.; Jia, S.; Zoou, J.; Wu, S.; Han, X. A facile preparation of Ag_2O/P25 photocatalyst for selective reduction of nitrate. *Appl. Catal. B* **2015**, *176*, 53–61. [CrossRef]

52. Han, Q.; Liu, Z.; Xu, Y.; Chen, Z.; Wang, T.; Zhang, H. Growth and Properties of Single-Crystalline γ-Fe_2O_3 Nanowires. *J. Phys. Chem. C* **2007**, *111*, 5034–5038. [CrossRef]

53. Idriss, H. On the wrong assignment of the XPS O1s signal at 531–532 eV attributed to oxygen vacancies in photo- and electro-catalysts for water splitting and other materials applications. *Surf. Sci.* **2021**, *712*, 121894. [CrossRef]

54. Wang, J.; Zhang, P.; Li, J.; Jiang, C.; Yunus, R.; Kim, J. Room-temperature oxidation of formaldehyde by layered manganese oxide: Effect of water. *Environ. Sci. Technol.* **2015**, *49*, 12372–12379. [CrossRef] [PubMed]

55. Zhang, C.; Li, Y.; Wang, Y.; He, H. Sodium-Promoted Pd/TiO_2 for Catalytic Oxidation of Formaldehyde at Ambient Temperature. *Environ. Sci. Technol.* **2014**, *48*, 5816–5822. [CrossRef] [PubMed]

56. Anderson, B.G.; Jenne, E.A.; Chao, T.T. The sorption of silver by poorly crystallized manganese oxides. *Geochim. Cosmochim. Acta* **1978**, *37*, 611–622. [CrossRef]

57. Dutov, V.V.; Mamontov, G.V.; Zaikovskii, V.I.; Vodyankina, O.V. The effect of support pretreatment on activity of Ag/SiO_2 catalysts in low-temperature CO oxidation. *Catal. Today* **2016**, *278*, 150–156. [CrossRef]

58. Carabineiro, S.A.C.; Bastos, S.S.T.; Orfao, J.J.M.; Pereira, M.F.R.; Delgado, J.J.; Fifueiredo, J.L. Carbon Monoxide Oxidation Catalysed by Exotemplated Manganese Oxides. *Catal. Lett.* **2010**, *134*, 217–227. [CrossRef]

59. Sushkevich, V.L.; Ivanova, I.I.; Taarning, E. Mechanistic Study of Ethanol Dehydrogenation over Silica-Supported Silver. *ChemCatChem* **2013**, *5*, 2367–2373. [CrossRef]

60. Liu, Q.; Bie, Y.; Qiu, S.; Zhang, Q.; Sainio, J.; Wang, T. Lehtonen, Hydrogenolysis of methyl heptanoate over Co based catalysts: Mediation of support property on activity and product distribution. *J. Appl. Catal. B* **2014**, *147*, 236–245. [CrossRef]

61. Liang, S.; Teng, F.; Bulgan, G.; Zong, R.; Zhu, Y. Effect of Phase Structure of MnO_2 Nanorod Catalyst on the Activity for CO Oxidation. *J. Phys. Chem. C* **2008**, *112*, 5307–5315. [CrossRef]

62. Jia, J.; Zhang, P.; Chen, L. The effect of morphology of α-MnO_2 on catalytic decomposition of gaseous ozone. *Catal. Sci. Technol.* **2016**, *6*, 5841–5847. [CrossRef]

63. Zhang, J.; Li, Y.; Zhang, Y.; Chen, M.; Wang, L.; Zhang, C.; He, H. Effect of Support on the Activity of Ag-based Catalysts for Formaldehyde Oxidation. *Sci. Rep.* **2015**, *5*, 12950. [CrossRef] [PubMed]

64. Lup, N.K.; Abnisa, F.; Ashri, W.M.; Daud, W.; Aroua, M.K. Temperature-programmed reduction of silver(I) oxide using a titania-supported silver catalyst under a H2 atmosphere. *J. Chin. Chem. Soc.* **2019**, *66*, 1443–1455. [CrossRef]

65. Savel'eva, A.S.; Vodyankina, O.V. Formation of the active surface of Ag/SiO_2 catalysts in the presence of FeO_x additives. *Russ J. Phys. Chem. A* **2014**, *88*, 2203–2208. [CrossRef]

66. Santos, V.P.; Carabineiro, S.A.C.; Bakker, J.J.W.; Soares, O.S.G.P.; Chen, X.; Pereira, M.F.R.; Órfão, J.J.M.; Figueiredo, J.L.; Gascon, J.; Kapteijn, F. Stabilized gold on cerium-modified cryptomelane: Highly active in low-temperature CO oxidation. *J. Catal.* **2014**, *309*, 58–65. [CrossRef]

67. Dotsenko, S.S.; Verkhov, V.A.; Svetlichnyi, V.A.; Liotta, L.F.; La Parola, V.; Izaak, T.I.; Vodyankina, O.V. Oxidative dehydrogenation of ethanol on modified OMS-2 catalysts. *Catal. Today* **2020**, *357*, 503–510. [CrossRef]

68. Idriss, H.; Seebauer, E.G. Effect of oxygen electronic polarisability on catalytic reactions over oxides. *Catal. Lett.* **2000**, *66*, 139–145. [CrossRef]

69. Hu, S.; Wang, Y.; Wang, W.; Han, Y.; Fan, Q.; Feng, X.; Xu, Q.; Zhu, J. Ag Nanoparticles on Reducible CeO_2(111) Thin Films: Effect of Thickness and Stoichiometry of Ceria. *J. Phys. Chem. C* **2015**, *119*, 3579–3588. [CrossRef]

70. Hoh, S.W.; Thomas, L.; Jones, G.; Willock, D.J. A density functional study of oxygen vacancy formation on α-Fe_2O_3(0001) surface and the effect of supported Au nanoparticles. *Res. Chem. Intermed.* **2015**, *41*, 9587–9601. [CrossRef]

71. An, N.; Wu, P.; Li, S.; Jia, M.; Zhang, W. Catalytic oxidation of formaldehyde over Pt/Fe_2O_3 catalysts prepared by different method. *Appl. Surf. Sci.* **2013**, *285*, 805–809. [CrossRef]

72. Wang, P.; Duan, J.; Wang, J.; Mei, F.; Liu, P. Elucidating structure-performance correlations in gas-phase selective ethanol oxidation and CO oxidation over metal-doped γ-MnO_2. *Chin. J. Catal.* **2020**, *41*, 1298. [CrossRef]

73. Chen, J.; Tang, X.; Liu, J.; Zhan, E.; Li, J.; Huang, X.; Shen, W. Synthesis and Characterization of Ag−Hollandite Nanofibers and Its Catalytic Application in Ethanol Oxidation. *Chem. Mater.* **2007**, *19*, 4292–4299. [CrossRef]

74. Wang, J.; Luo, H.; Liu, P. Highly dispersed gold nanoparticles on metal-doped α-MnO$_2$ catalysts for aerobic selective oxidation of ethanol. *Catal. Commun.* **2020**, *142*, 106030. [CrossRef]
75. Koltunov, K.Y.; Sobolev, V.I. Selective gas-phase oxidation of ethanol by molecular oxygen over oxide and gold-containing catalysts. *Catal. Ind.* **2012**, *4*, 247–252. [CrossRef]